



Research Article

# Sol–gel synthesis and characterization of calcium-deficient hydroxyapatite photocatalysts suitable for hydrogen production: influence of the drip rate in the photocatalytic activity

J. B. Rojas-Trigos<sup>1</sup> · V. Suárez-Quezada<sup>1,2</sup> · L. Lartundo-Rojas<sup>3</sup> · M. Suárez-Quezada<sup>2</sup>

© Springer Nature Switzerland AG 2019

## Abstract

In the present work, the sol–gel synthesis of calcium-deficient hydroxyapatite samples is reported, under four different drip rates, to investigate their effects on their photocatalytic activity in the water splitting reaction, under UV irradiation. The results of the structural and chemical composition characterizations show that the increase in the drip rate has a negative effect on the stoichiometry, inducing significant deficiencies in the calcium and oxygen content. Likewise, the values of the band gap and valence band energies were determined, showing a correlation between them, and the deficiencies of Ca, O and OH induced by the drip rate. Finally, the photocatalytic production of hydrogen in the presence of the synthesized samples was evaluated, showing in all cases production rates much higher than that obtained by using Degussa P25 as a photocatalyst, under the same conditions.

**Keywords** Hydroxyapatite · Optical properties · Photocatalysis · Sol–gel · Water splitting

## 1 Introduction

Nowadays, the global energy production system is mostly based on the combustion of fossil fuels, representing more than the 85% of the primary world energy production. The increasing worldwide demand of fuel has generated a growing research for alternative energy sources, and, in this direction, hydrogen has been considered as an ideal fuel for the future. Hydrogen itself is not toxic, and its combustion does not create any pollution or greenhouse gases. Currently, there are several techniques to produce hydrogen, such as employing nuclear reactors to energize hydrolysis reactors, combustion of fossil fuels, electrocatalytic processes, electrolysis, thermolysis and photocatalytic water splitting reactions [1–5]. Photocatalysis is considered as a key technology to generate hydrogen fuel, exploiting the absorption and energy conversion

mechanisms in irradiated semiconductor materials, to produce hole–electron pairs to split the water molecule, generating (primarily) hydrogen and oxygen; and since the work of Fujishima and Honda [6] on water splitting, thousands of papers have been published on the topic. There are several semiconductor oxides such as  $\text{TiO}_2$ ,  $\text{ZnO}_2$ ,  $\text{RuO}_2$ ,  $\text{NaTaO}_3$  and  $\text{CdS}$ , and transition metal oxides, which have been studied as catalysts. The photocatalytic hydrogen production requires essentially the photogeneration of hole–electron pairs, but under the restriction that the conduction band (CB) and valence band (VB) levels satisfy the energy requirements set it by the reduction and oxidation potentials of the  $\text{H}_2\text{O}$  molecule, respectively [7–9].

Hydroxyapatite,  $\text{Ca}_{10}(\text{PO}_4)_6(\text{OH})_2$  or HA has been employed more and more frequently as catalysts and catalyst support because, thermodynamically and chemically speaking, it exhibits great stability and there are several

✉ J. B. Rojas-Trigos, jroast@ipn.mx | <sup>1</sup>Instituto Politécnico Nacional, Centro de Investigación en Ciencia Aplicada y Tecnología Avanzada, Unidad Legaria, Av. Legaria No. 694, Col. Irrigación, C.P. 11500 Mexico City, Mexico. <sup>2</sup>Departamento de Química, ECOCATAL, CONACYT—Universidad Autónoma Metropolitana-Iztapalapa, Av. San Rafael Atlixco No. 186, C.P. 09340 Mexico City, Mexico. <sup>3</sup>Instituto Politécnico Nacional, Centro de Nanociencias y Micro-Nanotecnologías, UPALM, Zacatenco, C.P. 07730 Mexico City, Mexico.



SN Applied Sciences (2019) 1:1410 | <https://doi.org/10.1007/s42452-019-1465-5>

Received: 5 August 2019 / Accepted: 3 October 2019 / Published online: 15 October 2019

methodologies for its synthesis and modification, particularly by the sol–gel route [10–17]. In the field of photocatalysis, some HA-based compounds has been also reported as photocatalyst in the decomposition of dimethyl sulfide, methyl mercaptan and 2, 4 dichlorophenoxyacetic acid [18–22]. In addition, there are some reports of the formation of oxidative radical species as  $\cdot\text{O}^{3-}$  and  $\cdot\text{OH}$  over non-stoichiometric HA irradiated with UV light. In the field of the hydrogen production, as far as we know, the role of HA was ascribed merely as support of photocatalyst [23], being the HA-based compounds employed in pollution treatment applications [24], reason why the results here presented could be of significant relevance for the advance of the hydrogen production technology.

In the present work, samples of calcium-deficient hydroxyapatite (with chemical formula  $\text{Ca}_{10-x}(\text{HPO}_4)_x(\text{PO}_4)_{6-x}(\text{OH})_{2-x}$ ,  $0 < x < 1$ , CDHA) were synthesized by means of the sol–gel technique, using four different drip rates during synthesis; and the photocatalytic activity was evaluated on the water splitting by measuring the hydrogen production rate, for each case. The reactor uses alcohol–water mixtures under UV light ( $\lambda = 254 \text{ nm}$ ) for photocatalytic hydrogen production. In addition, the synthesized photocatalyst samples were characterized, by different techniques, determining the structure, chemical composition and optical properties of samples.

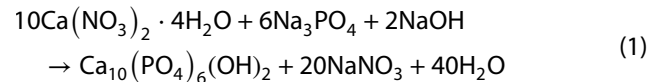
## 2 Materials and methods

For the synthesis of the calcium-deficient hydroxyapatite (CDHA) samples, the following chemical products were employed: calcium nitrate tetrahydrate ( $\text{Ca}(\text{NO}_3)_2 \cdot 4\text{H}_2\text{O}$ , purity  $\geq 99\%$ ), sodium phosphate ( $\text{Na}_3\text{PO}_4$ , 96% purity), both purchased from Sigma-Aldrich, and sodium hydroxide ( $\text{NaOH}$ , Merck; 0.02% K, max.). In addition, commercial Degussa P25 titanium dioxide ( $\text{TiO}_2$ ), nanopowder (Rutile/Anatase ratio content, 85:15)—20 nm primary particle size, purity  $\approx 99.9\%$  and an superficial area  $> 30 \text{ m}^2 \text{ g}^{-1}$  (data provided by the supplier)—was purchased through Integrated Nano-Science and Commodity Exchange (INSCX), to establish a comparison of the photocatalytic activity, between P25 and the here synthesized materials.

### 2.1 CDHA synthesis

As was mentioned in Sect. 1, several sol–gel methodologies can be found in the literature [10–17], some of them following an inorganic route [10–12, 16, 17], while others employ organic or organometallic precursors and/or organic surfactants [13–15]. In the here reported synthesis, the inorganic sol–gel route was chosen to avoid organic by-products. Anyway, some authors reported

methodologies maintaining a strict control of the pH during sol–gel synthesis [10, 15, 16], to ensure the formation of stoichiometric HA, whereas in others the pH evolution was unrestricted [11, 12]. In the present case, the induction of vacancies in the HA crystalline structure is sought by manipulating the pH during the synthesis, through varying the drip rate in the sol–gel synthesis of HA [12]. For this purpose, and considering Eq. (1), aqueous solutions of  $\text{Ca}(\text{NO}_3)_2 \cdot 4\text{H}_2\text{O}$ ,  $\text{Na}_3\text{PO}_4$  and  $\text{NaOH}$  were prepared at 0.1 M, using deionized (DI) water as solvent.



From the  $\text{NaOH}$  and  $\text{Na}_3\text{PO}_4$  aqueous solutions, a heterogeneous mixture was prepared and then added, drop-by-drop, to the aqueous solution of  $\text{Ca}(\text{NO}_3)_2 \cdot 4\text{H}_2\text{O}$  maintained under continuous stirring at room temperature ( $25 \text{ }^\circ\text{C}$ ). The resulting product was then filtered, obtaining a moist gel. After that, the moist gel was dried (in air atmosphere) at  $80 \text{ }^\circ\text{C}$  during 24 h, to eliminate the excess of DI water. The resulting xerogel was mechanically pulverized, to get a powdered sample of the synthesized compound. Using this procedure, four samples were synthesized at drip rates values of 5, 8, 10 and  $17 \mu\text{l s}^{-1}$ , named here as CDHA\_A, CDHA\_B, CDHA\_C and CDHA\_D samples, respectively.

### 2.2 Experimental details

The X-ray diffraction patterns of all samples were obtained by means of a Bruker X-ray diffractometer, model D-8 Advance, employing the Cu-K line ( $\lambda = 1.5418 \text{ \AA}$ ) and for diffraction angle ranging  $10^\circ \leq 2\theta \leq 70^\circ$ . The standard corundum powder pattern was used to determine the instrumental width,  $\beta_{\text{inst}} = 0.047^\circ$ , correcting the observed peaks width,  $\beta$ , by the corrected peak width  $\beta_c = (\beta^2 - \beta_{\text{inst}}^2)^{1/2}$ .

For the study of the elemental chemical composition of the samples, the energy-dispersive X-ray spectroscopy (XEDS) and the X-ray photoelectron spectroscopy (XPS) techniques were used to detect and quantify the chemical elements present in samples. The XEDS spectra were taken by means of a XEDS measurement system, integrated into a JEOL scanning electron microscope (model, JSM-6390LV), averaging over a focusing square surface of  $1200 \mu\text{m}$  wide, and for energy ranging 0.2–15 keV. The survey and high-resolution XPS spectrum was recorded for all samples, by using a K-Alpha X-ray photoelectron spectrometer (Thermo Fisher Scientific Company) with a monochromatic Al K $\alpha$  X-ray source, microfocused at the source to give a spot size of  $400 \mu\text{m}$ . The samples remain in the pre-chamber for 15 h and later transferred to the analytical chamber with a base pressure of  $1 \times 10^{-9}$  Torr. The

survey and high-resolution spectra were collected using analyzer pass energies of 200 and 20 eV, respectively, and in both cases, referenced according to the adventitious C1s peak. The analysis of the obtained data was performed by using Thermo Avantage software.

For the determination of the optical band gap,  $E_g$ , the Photoacoustic Spectroscopy (PAS) technique was employed here, for a photon wavelength  $206 \text{ nm} \leq \lambda \leq 288 \text{ nm}$  and for a modulation frequency,  $f = 17 \text{ Hz}$ . For that purpose, a home-made PAS measurement system was used, as represented schematically in Fig. 1. The continuous beam emitted by the 200-W Hg Arc lamp (Newport, Mod. 66483) optimized for UV passes through a monochromator (Newport, mod. Cornerstone 130 1/8 m) to obtain a quasi-monochromatic excitation beam. The continuous excitation beam was then modulated by a mechanical chopper (Stanford Research Systems, mod. SR-540), impinging into the optical window of the PAS measurement cell (MTEC, mod. 300). The PAS signal ( $S, \Delta\phi$ ) was then filtered and amplified by a lock-in amplifier (Stanford Research Systems, mod. SR 830), using the modulation frequency as reference, to be storage for its further analysis.

The minimum of the valence band,  $E_v$ , was determined from analysis of the XPS signals in the UV-photoelectron spectra region, recorded by means of the XPS measurement system previously described, for binding energy ranging  $-5$  to  $8 \text{ eV}$ .

The synthesized samples were used as photocatalysts for the production of hydrogen. The water splitting reaction was performed in a closed Pyrex glass reactor (200 ml capacity), connected by a piping system to a gas chromatograph (Gow Mac), to measure the hydrogen production during the reaction at regular time intervals. A UV Pen Ray lamp ( $254 \text{ nm}$ ,  $4.4 \text{ mW cm}^{-2}$ ), protected by a quartz tube

and enclosed in the Pyrex reactor, was used as excitation source. A schematic drawing of the reactor system is presented in Fig. 2.

### 3 Results and discussion

#### 3.1 Crystalline structure

Under the conditions described in Sect. 2.2, the X-ray diffraction pattern was acquired for all samples, finding good agreement with the ICDD published crystallographic charts 00-046-0905 and 00-026-1056, corresponding to CDHA and octacalcium phosphate ( $\text{Ca}_8\text{H}_2(\text{PO}_4)_6 \cdot 5\text{H}_2\text{O}$ , OCP), respectively (see Fig. 3). The Figure-of-Merit (FoM) values were up to 0.9, in all cases.

Other authors also reported the identified signals (Fig. 3) for OCP and CDHA [25–28]. As will be seen in the next section, the presence of CDHA and OCP is corroborated by XPS measurements. By means of the Scherrer's equation, an estimation of the crystallite size,  $D$ , is presented at next, analyzing the peaks corresponding to diffraction planes (2 0 1) and (0 0 2) of OCP and CDHA, respectively.

From Fig. 4 and Table 1, the peaks associated with (2 0 1) diffraction plane of the OCP component fit well to a Gaussian profile in all cases, while the peaks associated with (0 0 2) plane of the CDHA component are described by a Pseudo-Voigt profile. Concerning the Pseudo-Voigt profiles, the fitting procedures show shape factors of 0.80497, 0.87534, 0.78631 and 0.75362 for CDHA\_A, CDHA\_B, CDHA\_C and CDHA\_D samples, respectively. These values for the shape factor could be related to a particle-size effect in the powdered samples [29–31], due in part to the different drip rates employed during synthesis.

Fig. 1 Schematic drawing of the PAS measurement system

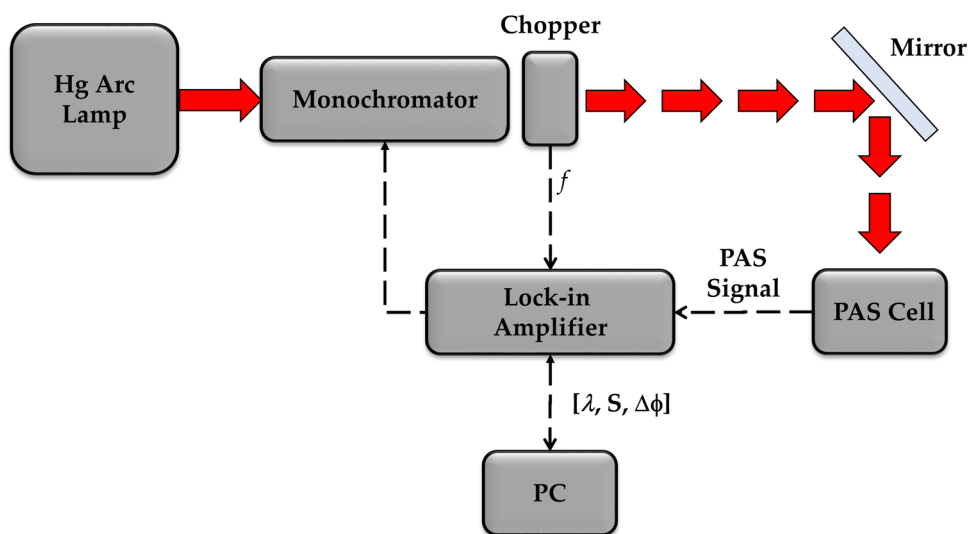


**Fig. 2** Schematic drawing of the hydrogen production system

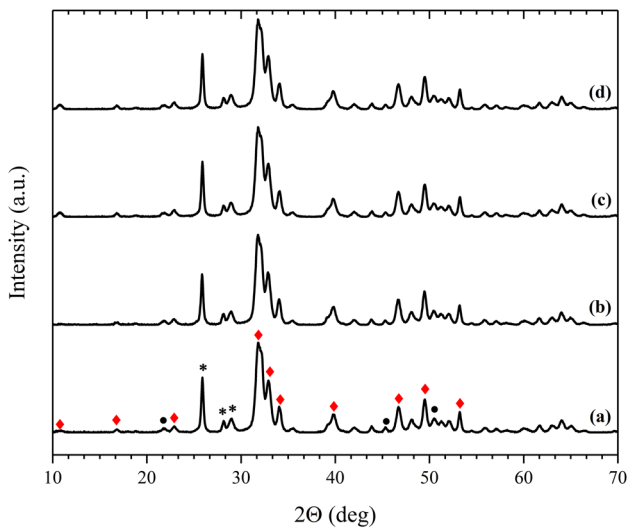
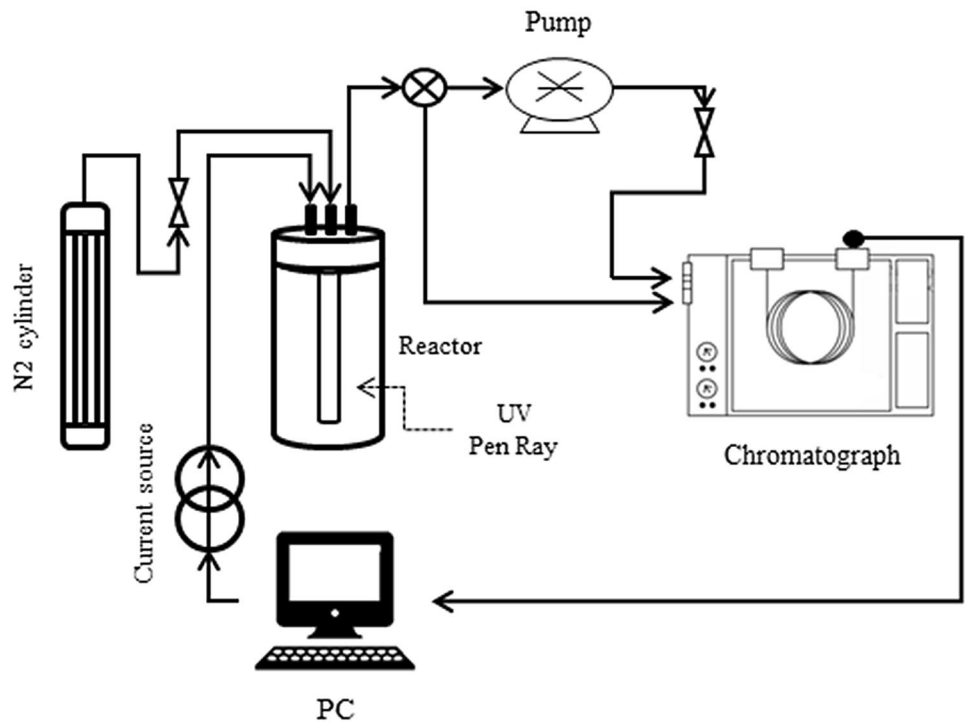


**Fig. 3** X-ray diffraction pattern of: (a) CDHA\_A, (b) CDHA\_B, CDHA\_C and (d) CDHA\_D samples. Asterisk—principal peaks associated with CDHA, circle—principal peaks associated to OCP, diamond—peaks related to both, CDHA and OCP

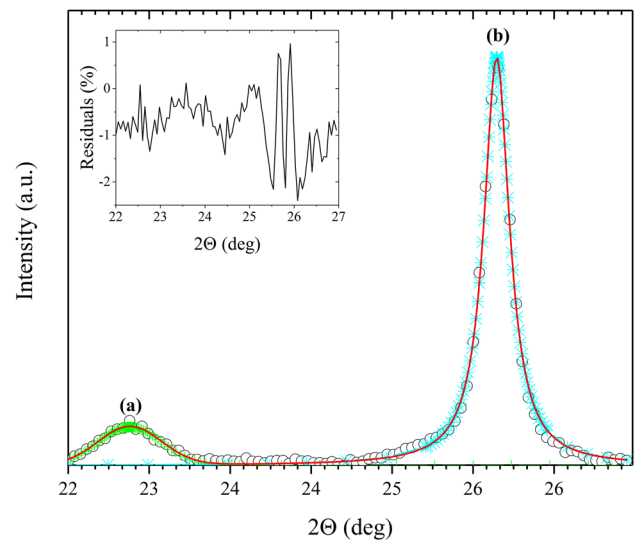


**Fig. 4** Excerpt of X-ray diffraction pattern of CDHA\_A sample, showing contributions due to: (a) plane (2 0 1) of OCP (green vertical dashes), and (b) plane (0 0 2) of CDHA (cyan cruces). The red solid line shows the best fitting

### 3.2 Elemental chemical composition

As was described in Sect. 2.2, the elemental chemical composition, in bulk, was determined from the corresponding XEDS spectrum of each sample, and the results are summarized in Table 2.

Considering the atomic ratios Ca/P and (Ca + O)/P for stoichiometric HA, it is noticed that the XEDS results agree with Ca-deficient hydroxyapatite in all cases [10–17, 32, 33], and that increasing the drip rate, the Ca/P and (Ca + O)/P ratios decrease monotonically. Moreover, the percentage difference between the obtained values for the Ca/P atomic ratios and the corresponding value for

**Table 1** Estimation of the crystallite size of the OCP and CDHA components

Sample	Peak center (°)		Peak type		Diffraction plane		$\beta_c$ (°)		$D$ (Å)	
	OCP	CDHA	OCP	CDHA	OCP	CDHA	OCP	CDHA	OCP	CDHA
CDHA_A	22.90	25.89	G	PV	(2 0 1)	(0 0 2)	0.562	0.263	144.20	309.77
CDHA_B	22.87	25.86	G	PV	(2 0 1)	(0 0 2)	0.616	0.272	131.68	299.40
CDHA_C	22.89	25.90	G	PV	(2 0 1)	(0 0 2)	0.588	0.254	137.76	320.36
CDHA_D	22.90	25.87	G	PV	(2 0 1)	(0 0 2)	0.349	0.229	232.51	356.15

G Gaussian, PV Pseudo-Voigt

**Table 2** Elemental chemical composition of the samples, by XEDS

Sample	Na (at.%)	C (at.%)	O (at.%)	P (at.%)	Ca (at.%)	Ca/P	(Ca + O)/P
CDHA_A	–	9.8	54.6	13.9	21.8	1.6	5.5
CDHA_B	–	7.4	56.9	14.6	21.1	1.5	5.4
CDHA_C	–	6.5	57.7	14.8	21.0	1.4	5.3
CDHA_D	0.2	8.6	57.3	14.4	19.5	1.3	5.3

stoichiometric HA changes dramatically as function of the drip rate, being a difference of 5.8% for CDHA\_A, while for CDHA\_B CDHA\_C and CDHA\_D samples the percentage differences rise to 12.9, 14.9 and 19.0%, respectively. A similar behavior is observed for the (Ca + O)/P ratio of samples, in comparison with the ideal value for HA, being the percentage difference of 8.3 and 10.7% for CDHA\_A and CDHA\_B samples, and 11.3% for the rest. Considering the previous remarks, and the observed content of oxygen, calcium and phosphorus, it can be concluded an important lack of oxygen and calcium in all samples, as the drip rate increases, being the oxygen lack dominant. Rojas-Trigos et al. reported these observed features in a previous work [12]; however, in the aforementioned work, the identification of oxygen lack as OH-vacancies was discussed only through the behavior of the energy band gap, remaining pendant the discussion about the presence of oxygen vacancies in the phosphate sites. Next, the survey of XPS spectra is displayed (Fig. 5), and the quantification results are summarized in Table 3.

From the results in Table 3, a similar tendency (respect to the drip rate) is observed in the superficial chemical composition, regarding the behavior of the atomic ratios Ca/P and (Ca + O)/P obtained by XEDS. Nevertheless, the observed changes in the percentage difference between the Ca/P and (Ca + O)/P ratio values of the samples, with respect to the ideal values for HA, are less abrupt. As with the bulk elemental quantification by XEDS, the results given by XPS show traces of sodium and high levels of carbon in samples (Tables 2, 3, respectively). While the presence of Na is expected from the precursor solutions, the high content of carbon is mostly due to the adsorption of atmospheric CO<sub>2</sub> during the synthesis procedure, since the entire process was performed in the presence of air. Yelten and Yilmaz [34] study the factors affecting the

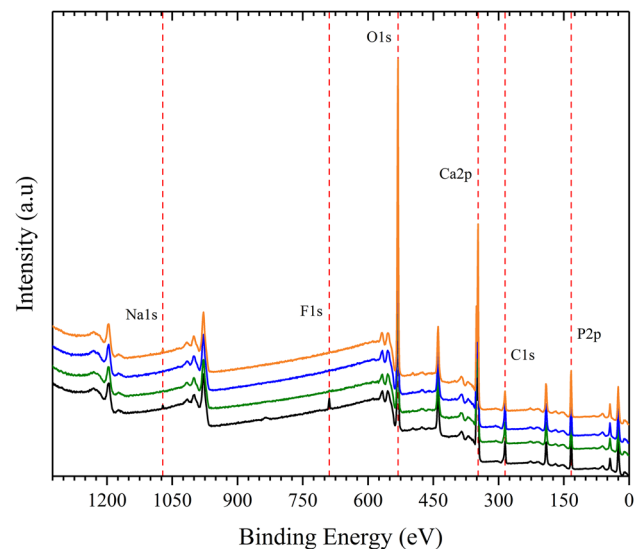


**Fig. 5** Survey XPS spectra of CDHA\_A (black line), CDHA\_B (green line), CDHA\_C (blue line) and CDHA\_D (orange line) samples. The vertical dashed lines mark the characteristic signals of the elements detected

HA synthesized by wet chemical precipitation technique, reporting the presence of carbonate ions due to absorption of atmospheric CO<sub>2</sub> during synthesis. Other authors have reported the presence of carbonate ions in HA synthesized by sol–gel technique [10–13, 17]; and it is worth mentioning that Rojas-Trigos and co-workers reported, in an earlier paper, that the CDHA samples achieved by the sol–gel procedure here employed exhibit a large specific area, ranging 91.85–101.85 m<sup>2</sup> g<sup>−1</sup>—depending on the drip rate value used for the synthesis procedure [12]—which enables the absorption of atmospheric CO<sub>2</sub>. The traces of fluorine, only detected by XPS, can only be



**Table 3** Elemental chemical composition of the samples, by XPS

Sample	F (at.%)	Na (at.%)	C (at.%)	O (at.%)	P (at.%)	Ca (at.%)	Ca/P	(Ca + O)/P
CDHA_A	1.9	0.4	13.4	54.8	12.4	17.1	1.4	5.8
CDHA_B	0.2	0.0	13.4	56.2	12.8	17.4	1.4	5.8
CDHA_C	0.1	0.1	14.6	55.5	12.8	17.0	1.3	5.7
CDHA_D	0.2	0.6	10.8	57.4	13.5	17.5	1.3	5.5

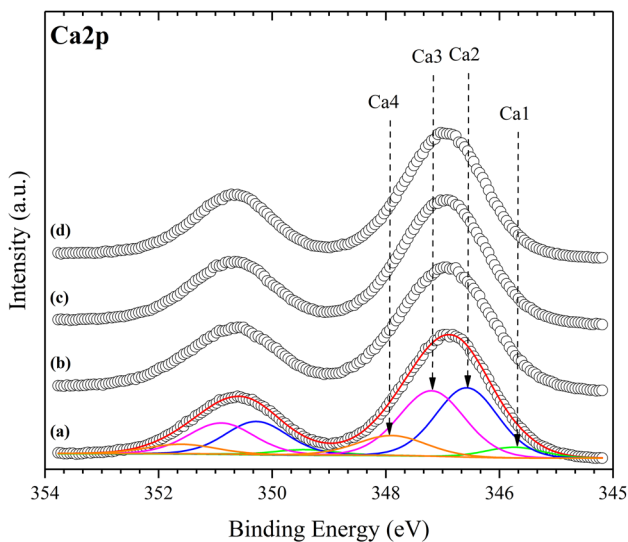


**Fig. 6** Calcium XPS high-resolution spectra of: (a) CDHA\_A, (b) CDHA\_B, (c) CDHA\_C and (d) CDHA\_D, showing the CaO (green line), CaCO<sub>3</sub> (blue line), DCPA+DCPD (magenta line), MCPM+FA+HA mixture (orange line) contributions. The red line shows the cumulative signal

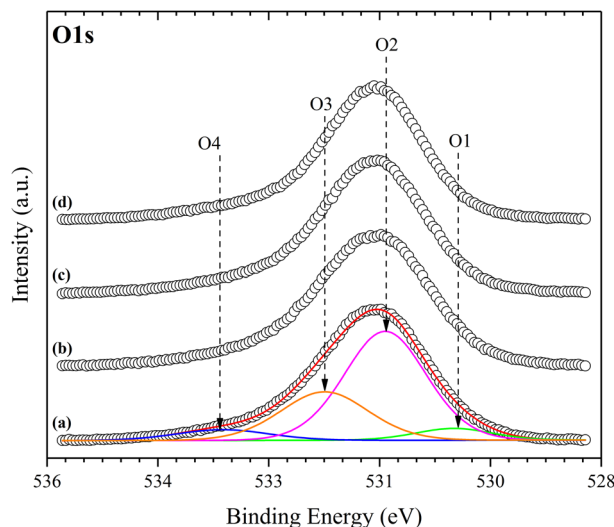


**Fig. 7** Oxygen XPS high-resolution spectra of: (a) CDHA\_A, (b) CDHA\_B, (c) CDHA\_C and (d) CDHA\_D, showing the CaO (green line), OH (blue line), DCPA+DCPD mixture (magenta line), CaCO<sub>3</sub>+MCPM+FA+HA mixture (orange line) contributions. The red line shows the cumulative signal

attributed to the water used during synthesis, which was acquired from a local supplier.

The high-resolution XPS measurements show a contribution to the spectra becoming from signals characteristic of several calcium phosphate compounds such as: HA; fluoroapatite (Ca<sub>10</sub>(PO<sub>4</sub>)<sub>6</sub>F<sub>2</sub>, FA); dicalcium phosphate anhydrous (CaHPO<sub>4</sub>, DCPA, also known as calcium hydrogen phosphate); dicalcium phosphate dihydrate (CaHPO<sub>4</sub>·2H<sub>2</sub>O, DCPD); monocalcium phosphate monohydrate (Ca(H<sub>2</sub>PO<sub>4</sub>)<sub>2</sub>·H<sub>2</sub>O, MCPM) and OCP [32, 33, 35–38]. In addition, there are signals of simpler calcium compounds contributing to the XPS spectra, such as calcium oxide, CaO, and calcium carbonate, CaCO<sub>3</sub> [39, 40], as shown in Figs. 6, 7 and 8.

In all regions (i.e., Ca2p, P2p and O1s), the presence of signals associated with HA and FA is observed, but considering the amounts of fluorine detected, the contribution of FA could be neglected with the one exception of CDHA\_A sample. The revealed presence of characteristic signals of DCPA, DCPD, MCPM and OCP is the second important feature, since they are HA precursors, via hydrolysis reactions under temperatures near or below the synthesis

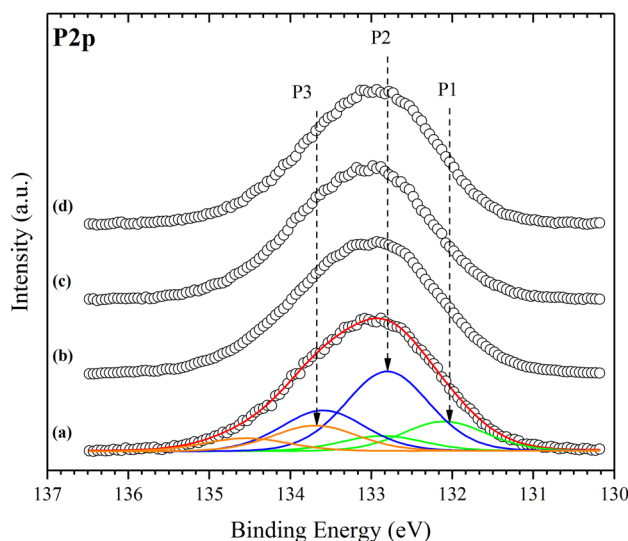


**Fig. 8** Phosphorus XPS high-resolution spectra of: (a) CDHA\_A, (b) CDHA\_B, (c) CDHA\_C and (d) CDHA\_D, showing the Na<sub>3</sub>PO<sub>4</sub> (green line), OCP (blue line), DCPA+DCPD+MCPM+FA+HA mixture (orange line) contributions. The red line shows the cumulative signal

and drying temperatures here employed (25 °C and 80 °C, respectively) [28, 41–45]. In Fig. 9, a better visualization of the wt% content of the calcium compounds, closely related to the apatite structure, is displayed.

Supported by Fig. 9b, d, higher drip rates hinder the formation of HA and CaO while promoting the formation of DCPA, DCPD, MCPM and OCP (see Fig. 9a, c), closely related to the formation of CDHA. At the same time, the quantification of the OH content (in wt%), from the O1s high-resolution spectra, shows an insignificant variance in the values of the sample set, being approximately 0.072 wt% with respect to the mean value 7.16 wt%. These results are consistent with the values of the Ca/P and (Ca + O)/P ratios (Tables 2, 3), supporting the idea that, along with the Ca vacancies, there is a lack on the oxygen content in the apatite structures, been significant the influence of the drip rate. Keeping in mind the results published by Rojas-Trigos et al. [12] on the pH behavior during the sol–gel synthesis as function of the drip rate, a close correlation

arises between the pH and the presence of O vacancies and/or OH vacancies.

### 3.3 Optical properties

Among the different parameters involving in the performance of a material to function as photocatalyst, the optical band gap,  $E_g$ , and the valence band energy,  $E_v$ , are fundamental to understand its ability to produce electron–hole pairs, needed for the production of reducing and/or oxidizing species which initialize the photocatalytic reactions. These optical properties depend entirely on the crystalline structure, and are strongly affected by the presence of crystalline defects, vacancies, self-interstitial atoms, and substitutional and interstitial impurity atoms. In the particular case of vacancy defects, an energy shift in valence and conduction energy bands has been observed in different materials [46–48], as consequence.

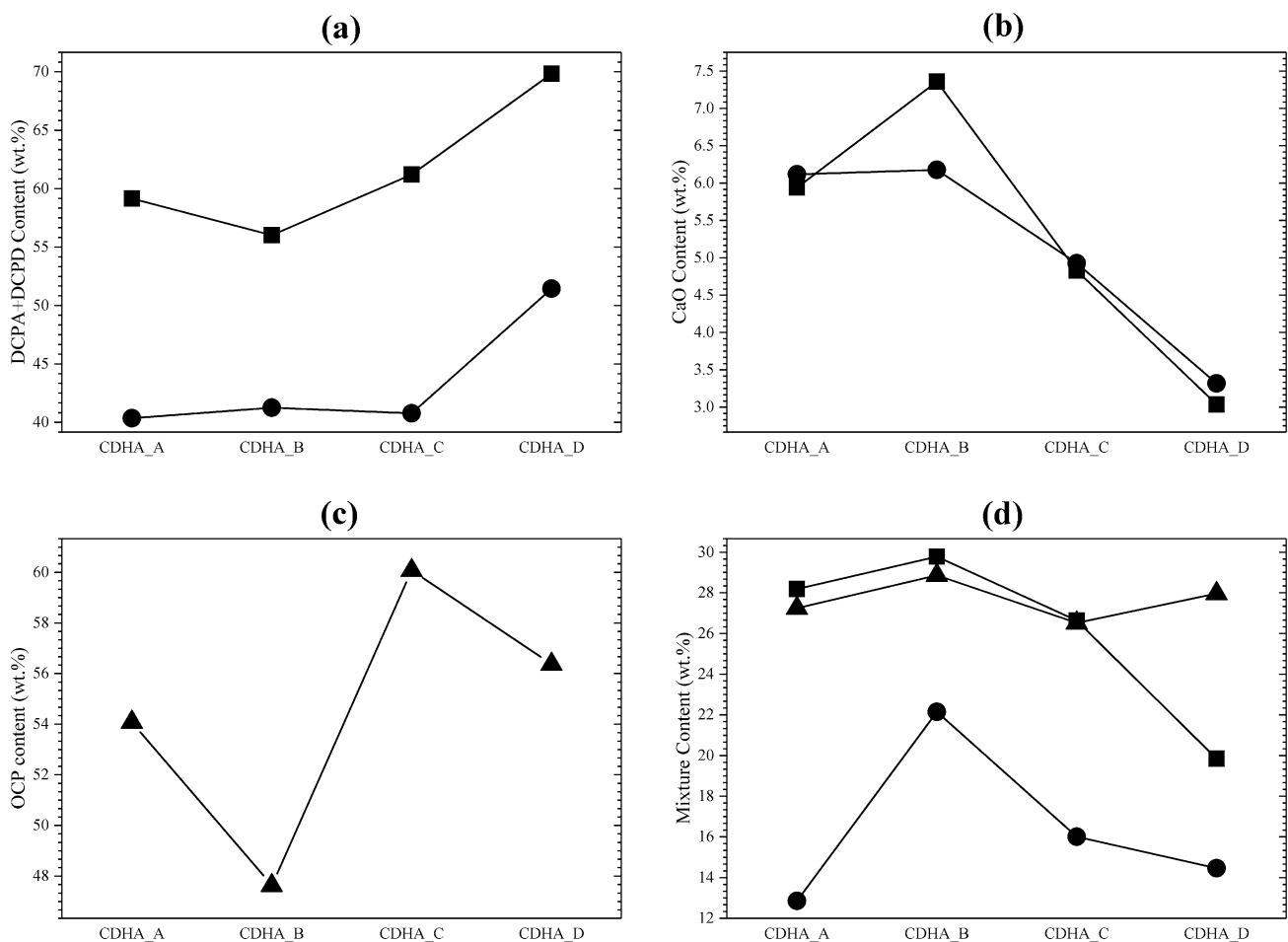


**Fig. 9** Content, in wt%, of: **a** DCPA+DCPD, **b** CaO, **c** OCP and **d** mixtures determined by the analysis of the Ca2p (black circles), O1s (black squares) and P2p (black triangles) high-resolution XPS spectra

### 3.3.1 Optical band gap determination

If the optical absorption spectrum is known, the optical energy band gap,  $E_g$ , can be estimated by constructing the Tauc plot  $h\nu$  versus  $[h\nu \cdot \alpha]^{1/2}$ —for an indirect band gap semiconductor, being  $h\nu$  the photon energy and  $\alpha$  the optical absorption coefficient—and extrapolating the linear region to the abscissa [49, 50]. A technique widely used to obtain the optical absorption spectrum is the Diffuse Reflectance Spectroscopy (DRS), in combination with the Kubelka–Munk theory [51], where the amplitude of the Kubelka–Munk function,  $F(R)$ , equals to the ratio  $\alpha \cdot \kappa^{-1}$ , where  $\kappa$  is the scattering coefficient. The PAS technique was chosen instead DRS technique, to obtain directly the optical absorption spectrum, since is less disturbed by light scattering effects than other optical spectroscopic techniques, including DRS, because the PAS signal is

generated only by the internal heat generation and diffusion in the sample, as result by the optical absorption and non-radiative thermal relaxation mechanisms [52, 53]. From the PAS data, and considering that the sample holder in the PA cell has a depth  $d=0.151$  cm, the optical absorption coefficient was estimated by the following expression:

$$\alpha(\lambda) = \ln(10) \cdot \left[ \frac{S(\lambda)}{d} \right] \tag{2}$$

In Fig. 10, the corresponding Tauc plot is presented for each sample, and analyzed by performing a linear extrapolation around the inflexion point, estimating the energy band gap.

The obtained values for  $E_g$  are consistent with the measured values reported elsewhere [54–56], and with the theoretical calculations performed by different techniques for

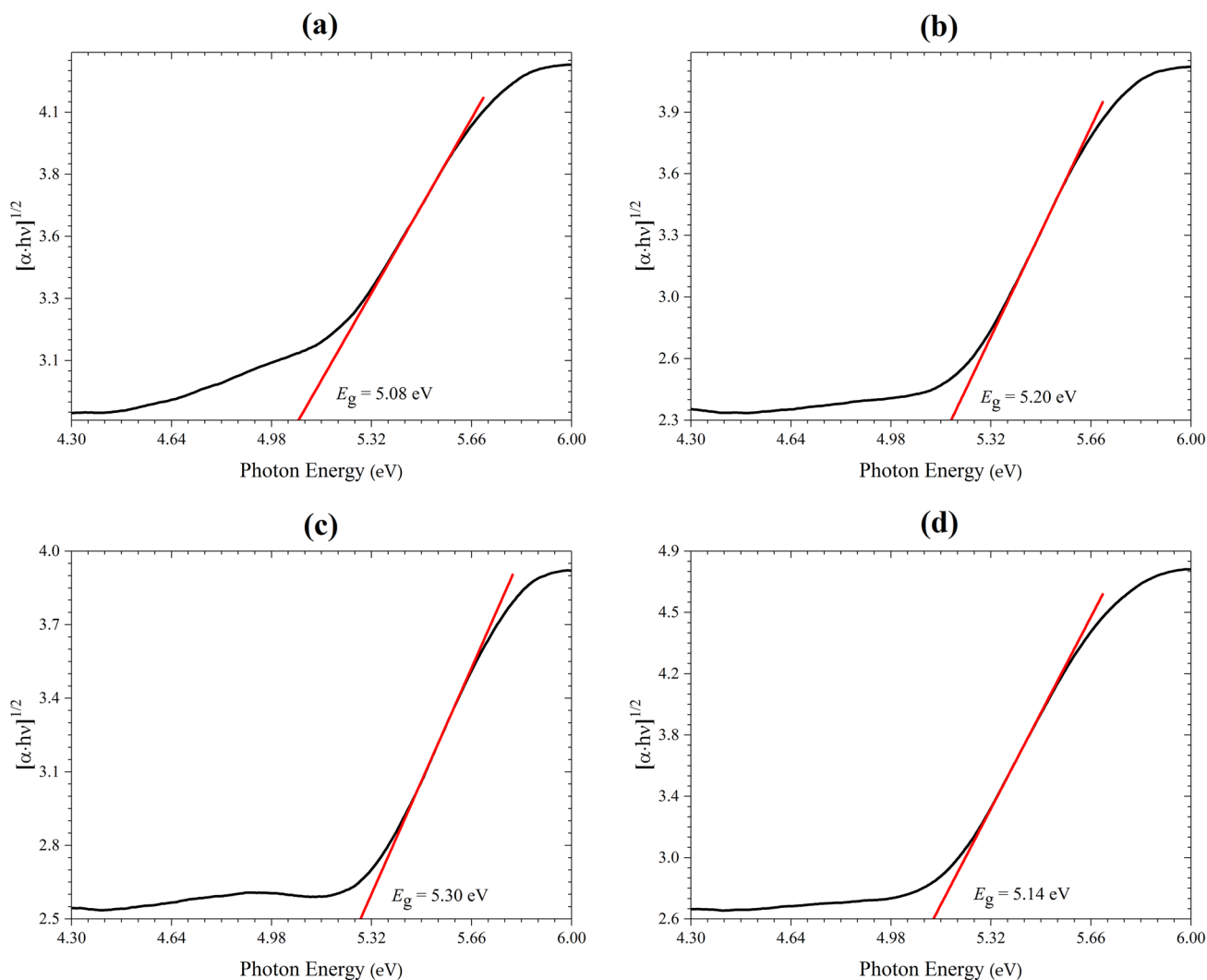


**Fig. 10** Tauc plot of: **a** CDHA\_A, **b** CDHA\_B, **c** CDHA\_C and **d** CDHA\_D. The red line shows the linear extrapolation



other authors [56–60]. All the aforementioned published works [56–60] agree that the common factor in the synthesis of non-stoichiometric hydroxyapatite is the presence of Frenkel, Schottky or anti-Schottky defects always involving Ca vacancies and interstitial  $\text{Ca}^{2+}$ , O and OH vacancies, and (possible) carbonate groups substituting  $\text{OH}^-$  and/or  $\text{PO}_4^{3-}$ . Considering the discussion done in Sect. 3.2, the PAS results and keeping in mind the influence of the possible defects in CDHA in the band structure [56], the behavior of the  $E_g$  values could be explained by the presence of Ca vacancies, coexisting with OH vacancies and interstitial OH ions. These crystalline defects are possible by changes in internal energy, due to the pH evolution, through the drip rate, during synthesis.

### 3.3.2 Maximum valence band energy determination

Closing this section, an analysis of the UV-photoelectron spectroscopic measurement was performed for each sample, determining the  $E_v$  values by a linear extrapolation near over the inflexion point in the leading edges, as shown in Fig. 11.

The behavior of the  $E_v$  energies, in relation to the increasing values of the drip rate, is exactly the opposite to the observed for the band gap values, showing a shift energy to lower values, as other authors reported for semiconductor structures exhibiting vacancies in their crystalline lattices [46–48]. From the PAS and UV-photoelectron spectroscopy measurements,  $E_g$  and  $E_v$  energies, and the conduction band minimum (CBM) are summarized in Table 4.

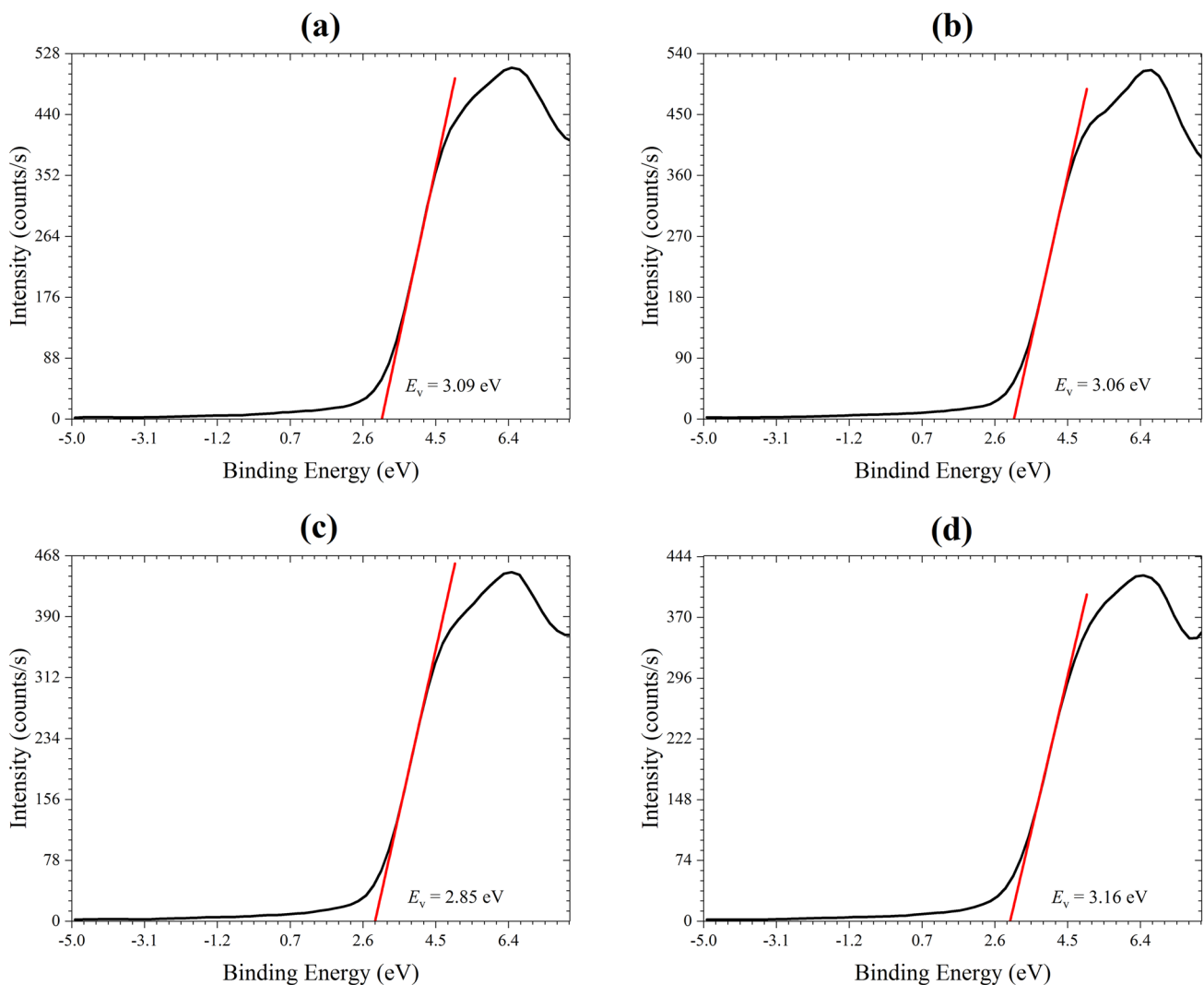


**Fig. 11** UV-photoelectron spectra of: **a** CDHA\_A, **b** CDHA\_B, **c** CDHA\_C and **d** CDHA\_D. The red line shows the linear extrapolation

**Table 4** Optical band gap, valence band energy and CBM of samples

Sample	$E_g$ (eV)	$E_v$ (eV)	CBM (eV)
CDHA_A	5.08	3.09	1.99
CDHA_B	5.20	3.06	2.14
CDHA_C	5.30	2.85	2.45
CDHA_D	5.14	3.16	1.98

The previous results are evidence that the synthesized samples tend to act as *n*-type, wide band gap semiconductors, supporting the presence of Ca vacancies. In addition, the CBM values place the Fermi level closer to the conduction band in CDHA\_A and CDHA\_D samples, than for CDHA\_B and CDHA\_C samples, which is consistent with the coexistence of O vacancies and OH vacancies, in such combination that CDHA\_A and CDHA\_D samples will tend to act more as reducing agents than oxidizing agents.

### 3.4 Hydrogen production efficiency

For the hydrogen production evaluation, a 150 ml of water–methanol solution (in a 1:1 volume ratio) was prepared. Then, 10 mg of synthesized CDHA was added to the water–methanol solution, partially filling up the reactor with the mixture. The reactor was purged with nitrogen, then sealed and connected to a diaphragm pump

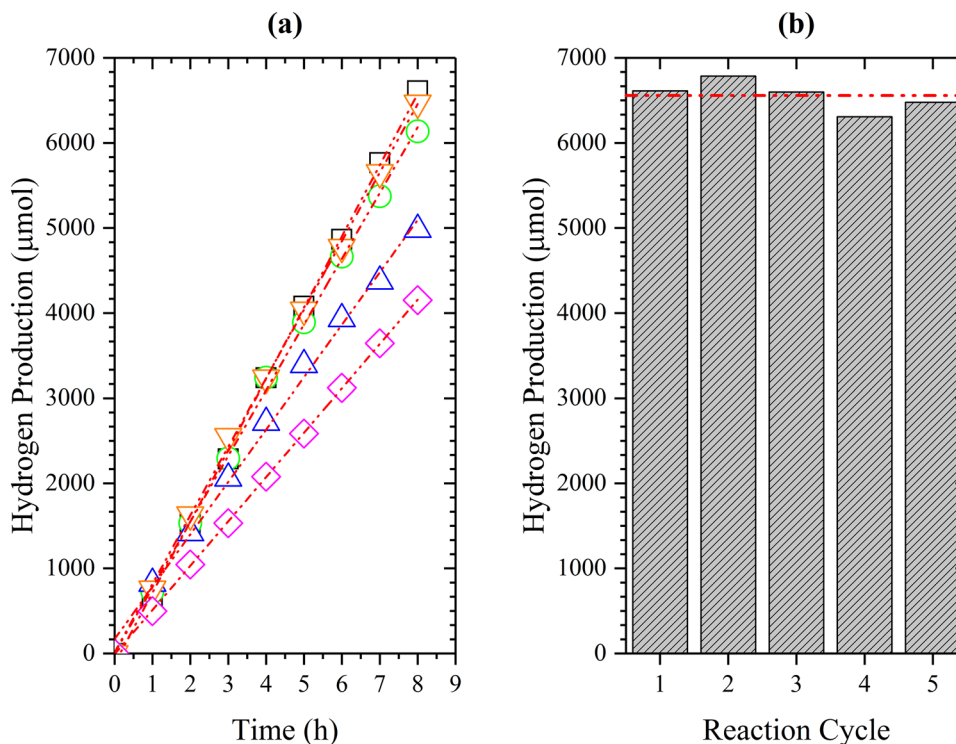
to inject the sample into the gas chromatograph. The amount of produced hydrogen, under UV irradiation in the presence of the photocatalyst, was measured every hour during an 8-h period. The stability of the photocatalytic hydrogen production (using sample CDHA\_A) under the same experimental conditions was assessed during five consecutive production cycles of 8 h. The results of the hydrogen production are summarized in Fig. 12 and Table 5, making a comparison between the performance of the samples and the standard P25 photocatalyst, under the same conditions.

As can be seen from the obtained results, the hydrogen production exhibits a linear evolution in all cases. Also, the production rate decreases as the Ca/P and (Ca + O)/P ratios decrease too, with the one exception of the CDHA\_D, which agrees with the coexistence of Ca, O and OH vacancies in CDHA\_A and CDHA\_D samples.

**Table 5** Hydrogen production, after 8 h, under UV irradiation

Sample	Maximal production ( $\mu\text{mol}$ )	Production rate ( $\mu\text{mol h}^{-1}$ )
CDHA_A	6611.04	815.62
CDHA_B	6135.17	773.28
CDHA_C	4980.52	645.44
CDHA_D	6469.65	807.77
P25	4151.96	520.92

**Fig. 12** **a** Hydrogen production in the presence of: CDHA\_A (black squares), CDHA\_B (green circles), CDHA\_C (blue up-triangles), CDHA\_D (orange down-triangles) and P25 (magenta diamonds) photocatalysts. The red dash-dotted lines show the best linear fittings. **b** Hydrogen production stability, in the presence of CDHA\_A photocatalysts. The red-dashed line shows the average production



Notice that all samples show higher hydrogen production rates, by 23.9 up to 56.6% (achieving the highest production with CDHA\_A sample), than the obtained by employing P25 as photocatalyst, and therefore a better performance in the water split reaction. For CDHA\_A sample, the mean hydrogen production value during the cycle evaluations was 6555.63  $\mu\text{mol}$ , with a standard error of mean of 78.96  $\mu\text{mol}$  (Fig. 12b). The maximal and minimal productions during the cycle evaluation were reached at the second and fourth cycles, respectively, occurring a recovery of 2.66% in the production at the end of the fifth cycle. The variations in the cycle-at-cycle productions could be assigned to adsorption–desorption processes, since the CDHA (and in general, apatite structures) exhibits a relatively large specific area. Particularly, it has been reported for the here studied samples, a specific area ranging 91.85–101.85  $\text{m}^2 \text{g}^{-1}$  [12], i.e., up to twofold the specific area reported for P25 and titanium compounds [61, 62]. Therefore, the CDHA\_A sample presents a stable efficiency in the photocatalytic water split reaction, under UV irradiation. Finally, it must be mentioned that the previous results for the CDHA\_A sample are competitive, even in comparison with those reported for other photocatalysts, such as ZnS–ZnO composites and  $\text{Bi}_2\text{S}_3$  nanorods supported on  $\text{ZrO}_2$  [63, 64].

## 4 Conclusions

The synthesis of hydroxyapatite-based photocatalyst samples was achieved, following a low-energy sol–gel route, employing four different drip rates. The structure and elemental chemical composition characterizations corroborate the presence of Ca-deficient hydroxyapatite along octacalcium phosphate and calcium hydrogenphosphate, which are precursors of Ca-deficient hydroxyapatite and tricalcium phosphate (which is a common by-product in Ca-deficient hydroxyapatite synthesis), being the stoichiometry of the synthesized samples strongly correlated to the drip rate. The optical characterizations show that all samples behave as *n*-type, wide band gap semiconductors, and the samples obtained from the lowest and highest drip rates synthesis tend to act more as reducing agents than oxidizing agents, due to the combined presence of calcium, oxygen and OH vacancies. Because of the presence of such crystalline defects, induced by the drip rates (and therefore, due to the pH during synthesis), all samples exhibit a superior hydrogen production than the titanium dioxide (P25), used here as standard. Particularly, the sample synthesized with the lowest drip rate has a very stable hydrogen production and 56.6% higher the standard under the same conditions.

**Acknowledgements** Authors acknowledge the Instituto Politécnico Nacional, Mexico, for financial support through 1855 SIP multidisciplinary and 20180376 SIP projects. The authors also wish to thank the Laboratorio Nacional de Conversión y Almacenamiento de Energía (LNCAE) of the Instituto Politécnico Nacional, Mexico, for helping with the acquisition of XRD data.

## Compliance with ethical standards

**Conflict of interest** On behalf of all authors, the corresponding author states that there is no conflict of interest.

## References

1. Al-Zareer M, Dincer I, Rosen MA (2017) Development and assessment of a novel integrated nuclear plant for electricity and hydrogen production. *Energy Convers Manag* 134:221–234
2. Gradisher L, Dutcher B, Fan M (2015) Catalytic hydrogen production from fossil fuels via the water gas shift reaction. *Appl Energy* 139:335–349
3. Ipsakis D, Kraia TZ, Marnello GE, Ouzounidou M (2015) An electrocatalytic membrane-assisted process for hydrogen production from  $\text{H}_2$ . *Int J Hydrog Energy* 40:7530–7538
4. Guo K, PrévotEAU A, Rabaey K (2017) A novel tubular microbial electrolysis cell for high rate hydrogen production. *J Power Sources* 356:484–490
5. Maeda K, Domen K (2010) Photocatalytic water splitting: recent progress and future challenges. *J Phys Chem Lett* 1(18):2655–2661
6. Fujishima A, Honda K (1972) Electrochemical photolysis of water at a semiconductor electrode. *Nature* 238:37–38
7. Oros-Ruiz S, Zanella R, López R et al (2013) Photocatalytic hydrogen production by water/methanol decomposition using Au/TiO<sub>2</sub> prepared by deposition–precipitation with urea. *J Hazard Mater* 263:2–10
8. Torres-Martínez LM, Gómez R, Vázquez-Cuchillo O et al (2010) Enhanced photocatalytic water splitting hydrogen production on RuO<sub>2</sub>/La:NaTaO<sub>3</sub>, prepared by sol–gel method. *Catal Commun* 12:268–272
9. Li J, Qian X, Peng Y, Lin J (2018) Hierarchical structure NiO/CdS for highly performance H<sub>2</sub> evolution. *Mater Lett* 224:82–85
10. Degirmenbasi N, Kalyon DM, Birinci E (2006) Biocomposites of nanohydroxyapatite with collagen and poly(vinyl alcohol). *Colloids Surf B* 48:42–49
11. Feng W, Mu-sen L, Yu-peng L, Yong-xin Q (2005) A simple sol–gel technique for preparing hydroxyapatite nanopowders. *Mater Lett* 59:916–919
12. Rojas-Trigos JB, Jiménez-Flores Y, Suárez V et al (2018) Sol–gel synthesis of calcium-deficient hydroxyapatite: Influence of the pH behavior during synthesis on the structural, chemical composition and physical properties. In: Cavalheiro AA (ed) *Powder technology*. In Tech d.o.o., Rijeka. ISBN 978-953-51-6219-3
13. Andersson J, Arevá S, Spliethoff B, Lindén M (2005) Sol–gel synthesis of a multifunctional, hierarchically porous silica/apatite composite. *Biomaterials* 26:6827–6835
14. Chen J, Wang Y, Chen X et al (2011) A simple sol–gel technique for synthesis of nanostructured hydroxyapatite, tricalcium phosphate and biphasic powders. *Mater Lett* 65(12):1923–1926
15. Chai CS, Gross KA, Ben-Nissan B (1998) Critical ageing of hydroxyapatite sol–gel solutions. *Biomaterials* 19:2291–2296
16. Anee TK, Ashok M, Palanichamy M, Narayana Kalkura S (2003) A novel technique to synthesize hydroxyapatite at low temperature. *Mater Chem Phys* 80:725–730

17. Jahandideh R, Behnamghader A, Rangie M et al (2009) Sol–gel synthesis of FHA nanoparticles and CDHA agglomerates from a mixture with a nonstoichiometric Ca/P ratio. *Key Eng Mater* 396–398:607–610
18. Nishikawa H (2004) A high active type of hydroxyapatite for photocatalytic decomposition of dimethyl sulfide under UV irradiation. *J Mol Catal A* 207:149–153
19. Nishikawa H, Omamiuda K (2002) Photocatalytic activity of hydroxyapatite for methyl mercaptane. *J Mol Catal A* 179:193–200
20. Pratap Reddy M, Venugopal A, Subrahmanyam M (2007) Hydroxyapatite photocatalytic degradation of calmagite (an azo dye) in aqueous suspension. *Appl Catal B* 69:164–170
21. Jiménez-Flores Y, Suárez-Quezada M, Rojas-Trigos JB et al (2017) Sol–gel synthesis of Tb-doped hydroxyapatite with high performance as photocatalyst for 2, 4 dichlorophenoxyacetic acid mineralization. *J Chem Technol Biotechnol* 92(7):1521–1530
22. Jiménez-Flores Y, Suárez-Quezada M, Rojas-Trigos JB et al (2017) Characterization of Tb-doped hydroxyapatite for biomedical applications: optical properties and energy band gap determination. *J Mater Sci* 52(17):9990–10000
23. Yaakob Z, Hakim L, Satheesh Kumar MN et al (2010) Hydroxyapatite supported Nickel catalyst for hydrogen production. *Am J Sci Ind Res* 1(2):122–126
24. Liu X, Ma J, Yang J (2018) Visible-light-driven amorphous Fe(III)-substituted hydroxyapatite photocatalyst: characterization and photocatalytic activity. *Mater Lett* 137:256–259
25. Ito N, Kamitakahara M, Ioku K (2014) Preparation and evaluation of spherical porous granules of octacalcium phosphate/hydroxyapatite as drug carriers in bone cancer treatment. *Mater Lett* 120:94–96
26. Suzuki O (2010) Octacalcium phosphate: osteoconductivity and crystal chemistry. *Acta Biomater* 6:3379–3387
27. Mandel S, Tas AC (2010) Brushite ( $\text{CaHPO}_4 \cdot 2\text{H}_2\text{O}$ ) to octacalcium phosphate ( $\text{Ca}_8(\text{HPO}_4)_2(\text{PO}_4)_4 \cdot 5\text{H}_2\text{O}$ ) transformation in DMEM solutions at 36.5 °C. *Mater Sci Eng C* 30:245–254
28. Arellano-Jiménez MJ, García-García R, Reyes-Gasga J (2009) Synthesis and hydrolysis of octacalcium phosphate and its characterization by electron microscopy and X-ray diffraction. *J Phys Chem Solids* 70:390–395
29. Finger LW, Cox DE, Jephcoat AP (1994) A correction for powder diffraction peak asymmetry due to axial divergence. *J Appl Cryst* 27:892–900
30. Sánchez-Bajo F, Cumbreira FL (1997) The use of the pseudo-Voigt function in the variance method of X-ray line-broadening analysis. *J Appl Cryst* 30:427–430
31. Baig AA, Fox JL, Young RA et al (1999) Relationships among carbonated apatite solubility, crystallite size, and microstrain parameters. *Calcif Tissue Int* 64:437–449
32. Chusuei CC, Goodman DW (1999) Calcium phosphate phase identification using XPS and time-of-flight cluster SIMS. *Anal Chem* 71:149–153
33. Kleine-Boymann M, Rohnke M, Henss A et al (2014) Discrimination between biologically relevant calcium phosphate phases by surface-analytical techniques. *Appl Surf Sci* 309:27–32
34. Yelten A, Yilmaz S (2016) Various parameters affecting the synthesis of the hydroxyapatite powders by the wet chemical precipitation technique. *Mater Today Proc* 3:2869–2876
35. Lu HB, Campbell CT, Graham DJ et al (2000) Surface characterization of hydroxyapatite and related calcium phosphates by XPS and TOF-SIMS. *Anal Chem* 72:2886–2894
36. Combes C, Rey C, Freche M (1998) XPS and IR study of dicalcium phosphate dihydrate nucleation on titanium surfaces. *Colloids Surf B Biointerfaces* 11:15–27
37. Landis WJ, Martin JR (1984) Xray photoelectron spectroscopy applied to gold-decorated mineral standards of biological interest. *J Vac Sci Technol A* 2(2):1108–1111
38. Demri B, Muster D (1995) XPS study of some calcium compounds. *J Mater Process Technol* 55:311–314
39. Ni M, Ratner BD (2008) Differentiating calcium carbonate polymorphs by surface analysis techniques—an XPS and TOF-SIMS study. *Surf Interface Anal* 40:1356–1361
40. Van Doveren H, Verhoeven JATH (1980) Xps spectra of Ca, Sr, Ba and their oxides. *J Electron Spectrosc Relat Phenom* 21:265–273
41. Francis MD, Webb NC (1971) Hydroxyapatite formation from a hydrated calcium monohydrogen phosphate precursor. *Calc Tissue Res* 6:335–342
42. Graham S, Brown PW (1996) Reactions of octacalcium phosphate to form hydroxyapatite. *J Cryst Growth* 165:106–115
43. Tsuru K, Yoshimoto A, Kanazawa M et al (2017) Fabrication of carbonate apatite block through a dissolution–precipitation reaction using calcium hydrogen phosphate dihydrate block as a precursor. *Materials* 10:374
44. Vallet-Regí M, Rodríguez-Lorenzo LM, Salinas AJ (1997) Synthesis and characterization of calcium deficient apatite. *Solid State Ion* 101–103:1279–1285
45. Mandel S, Tas AC (2010) Brushite ( $\text{CaHPO}_4 \cdot 2\text{H}_2\text{O}$ ) to octacalcium phosphate ( $\text{Ca}_8(\text{HPO}_4)_2(\text{PO}_4)_4 \cdot 5\text{H}_2\text{O}$ ) transformation in DMEM solutions at 36.5 °C. *Mat Sci Eng C* 30:245–254
46. Fan Xiaoxing, Chen Xinyi, Zhu Shaopeng et al (2008) The structural, physical and photocatalytic properties of the mesoporous Cr-doped  $\text{TiO}_2$ . *J Mol Catal A Chem* 284:155–160
47. Cai L, Feng C (2017) Effect of vacancy defects on the electronic structure and optical properties of GaN. *J Nanotechnol* 2017:6987430
48. Zhu HX, Zhou PX, Li X, Liu J-M (2014) Electronic structures and optical properties of rutile  $\text{TiO}_2$  with different point defects from DFT + U calculations. *Phys Lett A* 378:2719–2724
49. Tauc J (1968) Optical properties and electronic structure of amorphous Ge and Si. *Mater Res Bull* 3(1):37–46
50. Tauc J, Grigorovici R, Vanacu A (1966) Optical properties and electronic structure of amorphous germanium. *Phys Status Solidi B* 15(2):627–637
51. Nowak M, Kauch B, Szperlich P (2009) Determination of energy band gap of nanocrystalline SbSI using diffuse reflectance spectroscopy. *Rev Sci Instrum* 80:046107
52. Rosencwaig A (1978) Theoretical aspects of photoacoustic spectroscopy. *J Appl Phys* 49:2905–2910
53. McDonald FA, Wetsel GC (1978) Generalized theory of the photoacoustic effect. *J Appl Phys* 49:2313–2322
54. Aronov D, Chaikina M, Haddad J et al (2007) Electronic states spectroscopy of hydroxyapatite ceramics. *J Mater Sci Mater Med* 18:865–870
55. Tsukada M, Wakamura M, Yoshida N, Watanabe T (2011) Band gap and photocatalytic properties of Ti-substituted hydroxyapatite: comparison with anatase- $\text{TiO}_2$ . *J Mol Catal A* 338:18–23
56. Bystrov VS, Coutinho J, Bystrova AV et al (2015) Computational study of hydroxyapatite structures, properties and defects. *J Phys D* 48:195302
57. Calderín L, Stott MJ (2003) Electronic and crystallographic structure of apatites. *Phys Rev B* 67:134106
58. Rulis P, Ouyang L, Ching WY (2004) Electronic structure and bonding in calcium apatite crystals: hydroxyapatite, fluorapatite, chlorapatite, and bromapatite. *Phys Rev B* 70:155104
59. de Leeuw NH, Bowe JR, Jeremy Rabone JAL (2007) A computational investigation of stoichiometric and calcium-deficient oxy- and hydroxy-apatites. *Faraday Discuss* 134:195–214
60. Santos RDS, Rezende MVS (2014) Atomistic simulation of intrinsic defects and trivalent and tetravalent ion doping in hydroxyapatite. *Adv Condens Matter Phys* 2014:609024

61. Brzozowski E, Castro MS (2000) Synthesis of barium titanate improved by modifications in the kinetics of the solid state reaction. *J Eur Ceram Soc* 20:2347–2351
62. Wang X, Pehkonen SO, Rämö J et al (2012) Experimental and computational studies of nitrogen doped Degussa P25 TiO<sub>2</sub>: application to visible-light driven photo-oxidation of As(III). *Catal Sci Technol* 2:784–793
63. Piña-Pérez Y, Aguilar-Martínez O, Acevedo-Peña P et al (2018) Novel ZnS–ZnO composite synthesized by the solvothermal method through the partial sulfidation of ZnO for H<sub>2</sub> production without sacrificial agent. *Appl Catal B* 230:125–134
64. García-Mendoza C, Oros-Ruiz S, Ramírez-Rave S et al (2017) Synthesis of Bi<sub>2</sub>S<sub>3</sub> nanorods supported on ZrO<sub>2</sub> semiconductor as an efficient photocatalyst for hydrogen production under UV and visible light. *J Chem Technol Biotechnol* 92:1503–1515

**Publisher's Note** Springer Nature remains neutral with regard to jurisdictional claims in published maps and institutional affiliations.